Eur. Phys. J. C 2, 627–641 (1998)
DOI 10.1007/s100529800880

THE EUROPEAN PHYSICAL JOURNAL C

Spin observables in neutron-proton elastic scattering

A. Ahmidouch[1,a], J. Arnold[2], B. van den Brandt[3], M. Daum[3], Ph. Demierre[1], R. Drevenak[5], M. Finger[4,5], M. Finger,Jr.[5], J. Franz[2], N. Goujon-Naef[1], P. Hautle[3], R. Hess[1,b], A. Janata[5], J.A. Konter[3], H. Lacker[2], C. Lechanoine-Leluc[1,c], F. Lehar[6], S. Mango[3], C. Mascarini[1,d], D. Rapin[1], E. Rössle[2], P.A. Schmelzbach[3], H. Schmitt[2], P. Sereni[2], M. Slunecka[4,5], A. Teglia[1,3], B. Vuaridel[1]

[1] DPNC, Université de Genève, CH-1211 Genève 4, Switzerland
[2] Fakultät für Physik der Universität Freiburg, D-79104 Freiburg, Germany
[3] PSI, Paul-Scherrer-Institut, CH-5232 Villigen-PSI, Switzerland
[4] MFF, Karlova Universita, CZ-18000 Praha, Czech Republic
[5] Joint Institute for Nuclear Research, RU-141980 Dubna, Russia
[6] CEA DAPNIA/SPP, CE-Saclay, F-91191 Gif-sur-Yvette (CEDEX), France

Received: 27 January 1998 / Published online: 30 March 1998

Abstract. The analyzing power, A_{oono} , and the polarization transfer observables K_{onno}, $K_{os''so}$ and $K_{os''ko}$ have been measured in neutron-proton elastic scattering at 260, 318, 386, 472 and 538 MeV for c.m. scattering angles between 64° and 160°. The data were obtained at PSI with a polarized neutron beam and a polarimeter analyzing the transverse polarization of the outgoing proton. They make a significant impact on the knowledge of the Isospin I =0 nucleon-nucleon scattering.

1 Introduction

In an attempt to understand better the Nucleon-Nucleon (NN) interaction at intermediate energies up to a few GeV, polarization phenomena have been studied in great detail over the past several decades.

Between 1975-1985, there was a large world-wide experimental effort on the study of pp elastic scattering, providing a complete and precise data base. From 1985 on, a similar effort was made to study the np reaction which, at that time, was poorly known. In addition, data taken under similar conditions were sometimes inconsistent [1]. At three different laboratories, PSI, LAMPF and SATURNE, systematic studies of the np elastic scattering reaction leading to complete experiments have been undertaken, each laboratory studying in a well-defined energy range, PSI between 250 and 550 MeV, LAMPF between 480 and 800 MeV and SATURNE between 800 and 1100 MeV. At the TRIUMF laboratory, below 500 MeV, more emphasis was put on experiments testing the fundamental symmetries, like charge symmetry and parity conservation, and a less extensive set of np experiments was performed. All this research, which has now come to an end, has been extremely successful and has brought a wealth of new data.

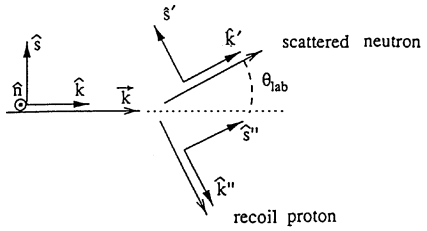

Fig. 1. Definition of spin directions for the beam, target, forward-scattered and recoil particles for nucleon-nucleon elastic scattering

From these accurate and diverse data, a precise phase shift determination can be performed and a direct reconstruction of the scattering amplitudes can even be done without any theoretical input other than symmetry laws.

Throughout this paper we will use the scattering matrix and formalism of [2]. For experimental observables, we use a four-index notation X_{srbt}, the subscripts referring to the scattered(s), recoil(r), beam(b) and target(t) spin orientations, respectively. Each index (s,r,b or t) can take on the values k,n,s or 0 according to the particle polarization orientation in its attached laboratory frame. The direction $\hat{k}$ is defined as being along the particle trajectory, $\hat{n}$ along the normal to the scattering plane and $\hat{s}$ is orthogonal to the other two axes ($\hat{n} \times \hat{k}$). The 0 index stands for an unpolarized state. Where confusion can occur, indices for the recoil particle will be indicated by double primes, i.e s'', n'' ($n'' \equiv n$) and k'', and those for the scattered particle

[a] *Present address*: MIT, Cambridge, MA 02139, USA
[b] Deceased
[c] e-mail: catherine.leluc@physics.unige.ch
Tel.: +41 22 702 62 45; Fax: +41 22 781 21 92
[d] *Present address*: Hopital Cantonal de Genève, Division de Pathologie Clinique, 1 rue M. Servet, 1211 Geneva 4, Switzerland

with primes, i.e s' , n' ($n' \equiv n$) and k', as explained in Fig. 1.

For an arbitrary reaction of the type $\frac{1}{2} + \frac{1}{2} \rightarrow \frac{1}{2} + \frac{1}{2}$, there are 256 possible independent observables. However, if parity conservation, the generalized Pauli principle and time reversal invariance are assumed, there remain only 25 linearly-independent observables. All these scattering observables can then be expressed as bilinear combinations of the five amplitudes describing the scattering matrix, namely *a,b,c,d* and *e* which are complex functions of two variables, e.g the energy and the c.m. scattering angle. For instance, the spin observables presented in this paper are given in the laboratory system by

$$\sigma \equiv \mathrm{d}\sigma/\mathrm{d}\Omega = \tfrac{1}{2}(|a|^2 + |b|^2 + |c|^2 + |d|^2 + |e|^2) \quad (1)$$

$$\sigma A_{oono} = \mathrm{Re}(a^* e) \quad (2)$$

$$\sigma K_{onno} = \tfrac{1}{2}(|a|^2 - |b|^2 + |c|^2 - |d|^2 + |e|^2) \quad (3)$$

$$\sigma K_{os''so} = -\mathrm{Re}(a^* c)\cos(\theta^\star + \theta_2) - \mathrm{Re}(b^* d)\cos(\theta_2) + \mathrm{Im}(c^* e)\sin(\theta^\star + \theta_2) \quad (4)$$

$$\sigma K_{os''ko} = \mathrm{Re}(a^* c)\sin(\theta^\star + \theta_2) - \mathrm{Re}(b^* d)\sin(\theta_2) + \mathrm{Im}(c^* e)\cos(\theta^\star + \theta_2) \quad (5)$$

where $\theta^\star$ is the c.m. scattering angle and θ_2 the laboratory angle of the recoil particle [2]. Only the measurement of spin observables can give the necessary insight into the relative contributions of these amplitudes, while the knowledge of the differential cross-section provides the absolute normalization of the amplitudes. In the bilinear products of amplitudes, an overall phase cancels out in the expression of an observable. This phase remains undetermined in the amplitude reconstruction.

An unambiguous determination of the five isospin-one (I=1) and five isospin-zero (I=0) elastic scattering amplitudes requires a large number of measurements of different spin parameters at each scattering angle and energy. More than nine observables in both the proton-proton (*pp*) and neutron-proton (*np*) systems are required to determine the five amplitudes unambiguously, up to an overall phase. The I=1 elastic scattering amplitudes are fairly well known up to 1 GeV from *pp* elastic scattering experiments, in particular from our previous work at PSI [3] and from SATURNE II [4]. On the other hand, the I=0 amplitudes were until recently poorly known for many reasons:

1. significant numbers of *np* differential cross-sections and polarization measurements have existed for some time, but until recently only a few measurements of other spin observables were available.
2. *pp* and *nn* elastic scattering are pure I=1 channels, whereas the *np* elastic scattering is a mixture of I=0 and I=1 channels. For any of the five amplitudes (*a, b, c , d* or *e*) one has

$$Amp(np, \theta^\star, T_o) = \tfrac{1}{2}[Amp(I = 0, \theta^\star, T_o) + Amp(I = 1, \theta^\star, T_o)] \quad (6)$$

where T_o is the incident kinetic energy. The factor of 1/2 in the equation above implies that the I=0 amplitudes will generally be more poorly determined from the *np* scattering than the I=1 amplitudes from *pp* scattering, assuming that the *pp* and *np* spin observables are measured to the same accuracy.
3. The I=0 amplitudes are obtained from (6) once the I=1 and *np* amplitudes are determined (up to an overall phase). At least one observable measured at the angle $\pi - \theta^\star$ is necessary in order to compute the relative phase between the *pp* and *np* amplitude system [5].

The *NN* amplitudes and phase shift values have proven to be a stringent test of theoretical models. One of the most successful models has been the meson-exchange model: the long-range part is mediated via one-pion exchange and the medium-range part by heavier mesons, (ρ, ω) or correlated-particle exchange such as that from two pions; the short range is described phenomenologically. Another considerable effort is presently devoted to the understanding of the nuclear force in terms of the quark model and QCD. Once again, the *NN* scattering amplitudes and phase shifts provide the critical tests for the quark-model calculations.

In this paper, we present results for the analyzing power, A_{oono} , and three different polarization transfer parameters K_{onno}, $K_{os''ko}$ and $K_{os''so}$, measured with a polarized beam and a CH_2 target. Preliminary results have been reported in conferences [6]. Details can be found in [7]. In Sect. 2 we describe the apparatus and associated electronics. Section 3 gives details about the analysis and Sect. 4 about the statistical estimators used. Section 5 presents the results and a comparison with available data [8-25] , different phase shift predictions [26,27] and potential models [28,29].

Other spin-dependent observables have also been measured with the same setup, but with a polarized target. These data, which require a different analysis as described in [30], will be presented in a separate article.

2 Experimental apparatus

2.1 Polarized neutron beam

We made use of the polarized neutron beam available at PSI in the NA2 area. A detailed description of the nucleon facility at PSI can be found in [31].

The polarized neutrons are produced at 0° in the reaction ^{12}C(**p**,**n**)X using longitudinal polarization transfer. The beam layout is sketched in Fig. 2. The 590 MeV primary proton beam with an intensity of 10 μA and with a vertical polarization of about 75% produced by the PSI cyclotron complex was used. The beam polarization in the cyclotron is vertical, and is reversed every second. A superconducting solenoid with longitudinal field (SOL) and a magnetic deflection (ACDY2) of 31° are used to produce longitudinally polarized protons. The neutrons are produced in a 12 cm long carbon target (1.75 g/cm^3 density). The remaining protons and other charged particles are swept out of the beam into a beam dump by a dipole

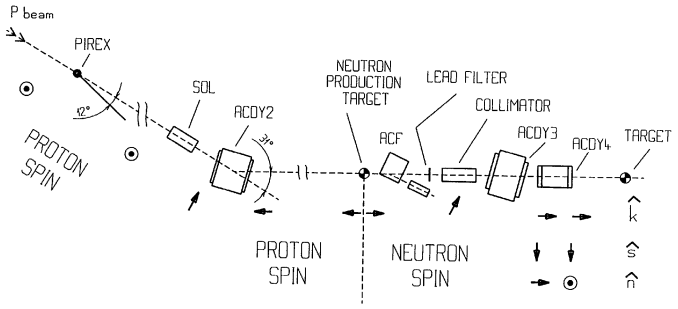

Fig. 2. Schematic lay-out of the PSI polarized neutron beam channel (not to scale). Only the critical elements used for the polarized neutron beam are indicated on the figure. The orientations of the proton and neutron spins at the various stages in the beam line are shown as *arrows*

magnet (ACF). A Pb filter attenuates the flux of photons coming from the decay of neutral pions (π^os) produced in the target. For data taking, we used a 30 mm thick absorber reducing the γ intensity by a factor 17 while only reducing the neutron intensity by 25%. A two meter long iron collimator (COL) with bores of various diameters is located downstream of the Pb filter. We used bores with diameters of 9 and 12 mm, defining beam spots with 27 and 36 mm diameter at the experimental target, respectively. A set of two spin precessing magnets (ACDY3 and ACDY4) with vertical and horizontal fields allows arbitrary rotation of the neutron polarization vector, in particular longitudinal $\hat{k}$, sideway $\hat{s}$ and vertical $\hat{n}$ (see Fig. 2.). These magnets also sweep out the charged particles produced by the lead filter or by the collimator.

The neutron beam is not monochromatic as seen in Fig. 3a. Since the primary proton beam is bunched at 50.63 MHz in packets of ∼1 ns wide, the energy of the incoming neutron at the experimental target can be determined event-by-event using time-of-flight. With a proton intensity of 10 μA, the neutron flux is $\sim 4.10^6 s^{-1} cm^{-2}$ at the experimental target placed 13.735 m downstream of the production target. The neutron polarization, as measured in a dedicated experiment [32], is shown in Fig. 3b. The beam polarization, P_b, is energy dependent, rising from 20% at 250 MeV to 45% at 560 MeV with some structure between 450 and 550 MeV. This dependence, although not yet understood, was also observed in a similar reaction performed at 795 MeV at LAMPF [33].

2.2 Beam monitoring

Several devices were used to monitor the polarization, the intensity and the position of the beam.

2.2.1 Proton polarimeter

A one-arm polarimeter is installed in the proton beam at the PIREX target station [31,34] (see Fig. 2.). It consists of a 1-mm-thick carbon target viewed by a scintillator telescope which counts particles scattered at an angle of 12°.

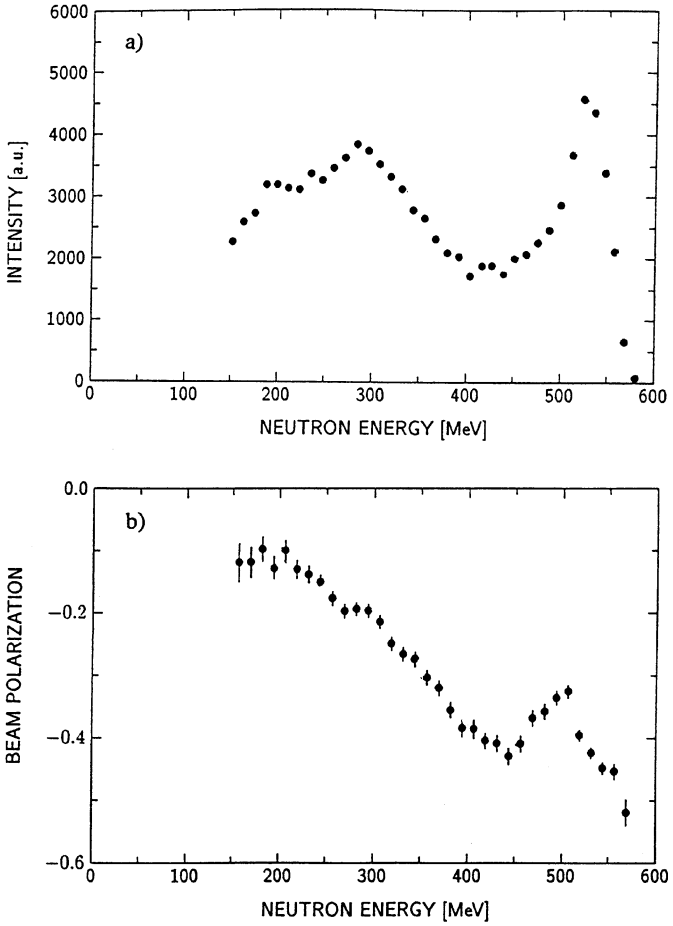

Fig. 3. a Energy spectrum of the neutron beam produced by scattering at 0°, **b** Neutron beam polarization as a function of the neutron kinetic energy

It is used to monitor eventual fluctuations of the proton beam polarization and consequently those of the neutron beam polarization.

2.2.2 Neutron intensity monitor (Monitor-1)

A neutron intensity monitor is placed in front of the experiment as shown in Fig. 4. It consists of a 12-mm-thick polyethylene target (CH_2) for conversion of neutrons into charged particles (recoil protons) which are counted by a coincidence $\overline{M_1} \cdot M_2 \cdot M_3$. This counting rate provides a relative measurement of the neutron beam intensity for normalization purposes. A Pb plate is used to convert some of the photons present in the neutron beam into electron-positron pairs for timing purposes (see Sects. 2.4.4 and 3.3.1). The last counter of Monitor-1 (M_3) is used to veto charged particles in the beam for the measurement of *np* scattering.

2.2.3 Neutron profile and polarization monitor (Monitor-2)

A second monitor is placed in the beam line six meters downstream of the NA2 target location. It consists of

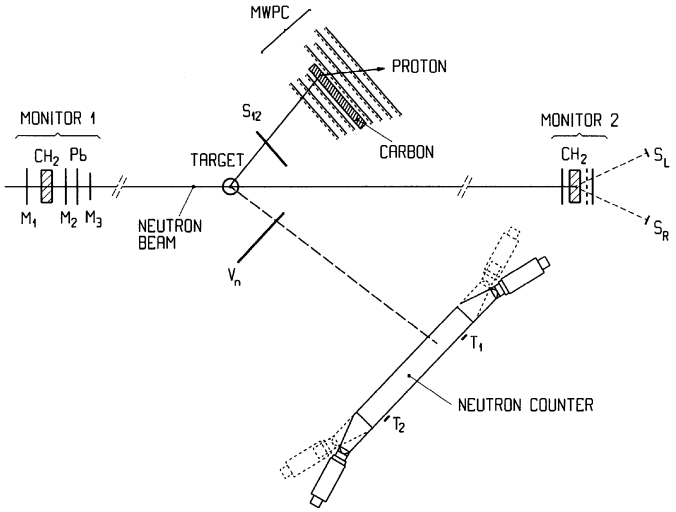

Fig. 4. Schematic view of the experimental setup (not to scale). M_1,M_2, M_3, V_n, S_{12}, T_1 and T_2 are scintillation counters. The two beam monitors (Monitor-1 and Monitor-2), placed up-stream and down-stream of the experiment, are indicated with a more expanded scale than the main detector

four consecutive layers: a thin Veto counter, a 1-cm-thick CH_2 converting target, and two orthogonal (X,Y) plastic scintillator hodoscopes which detect in coincidence the secondary emitted protons (see Fig. 4.). Each of the hodoscopes is made of five 3-cm-wide finger counters. In addition to this profile monitor, four counters S_U, S_D, S_L, S_R (up, down, left and right, respectively) detect protons scattered from the converter at an angle of 30°. These counters, in coincidence with the central X and Y fingers, provide four counting rates used to monitor the transverse components of the neutron beam polarization. At the same location, a monitor was installed which was used to center the neutron beam at the experimental scattering target [35].

2.3 Experimental setup

The experimental setup is sketched in Fig. 4. Both the scattered neutron and the recoil proton were measured by large acceptance detectors mounted on movable platforms. Two angular positions were used for the data taking: "A" with the neutron and proton arms at 44.1° and 41° respectively, for an angular range from 64° to 124° in the center of mass; "B" with the neutron and proton arms at 65° and 25° respectively, for an angular range from 104° to 164° in the center of mass.

2.3.1 Targets

The experimental target was located 13.735 m downstream of the neutron production target station. A cylindrical vertical CH_2 target with 2.5 cm diameter was used. A graphite target with similar dimensions as for the CH_2 target was used for background subtraction.

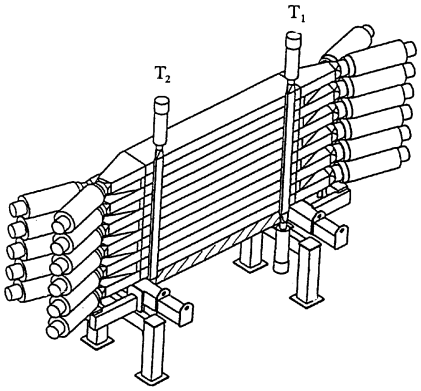

Fig. 5. Three-dimensional view of the neutron counter

2.3.2 Neutron arm

The neutron detector is shown in Fig. 5. It consisted of a wall made of 11 plastic scintillator bars with dimensions $130 \times 20 \times 8$ cm^3 placed 2.3 m from the center of the turn-table. The scintillation light caused by charged particles produced by the neutron interaction was detected by two XP2040 photomultipliers mounted at the ends of each bar. The horizontal coordinate of a neutron interaction was obtained from the timing difference between the two PM signals. A detailed description of these detectors with their associated electronics can be found in [36]. The background originating from natural radioactivity is not negligible when one uses such a large volume detector; therefore the thresholds given by the high voltage and the discriminators were set around 1 MeV$_{ee}$ (thresholds are expressed in absolute light units, the MeV electron equivalent, MeV$_{ee}$). Two additional scintillation counters T_1 and T_2 (1 cm thick, 6 cm wide, viewed by two XP2020 PMs) were placed vertically one meter apart directly behind the wall. They were used for the calibration of the reconstructed horizontal position of the interaction and for the relative timing offsets of the bars. The scintillation counter V_n, placed between the target and the neutron wall, was used to veto charged particles (see Fig. 4).

2.3.3 Proton arm

The proton arm consisted of:

1. a scintillation counter S_{12} (start), viewed by two PMs, used to detect the recoil proton for trigger purposes and for TOF measurements.
2. a polarimeter made of seven x and y multiwire proportional chambers (MWPC). The trajectories of the proton before and after a carbon scatterer were measured by two telescopes of equidistant MWPC. Three MWPC (640×380 mm^2) were in front of the carbon analyzer, four MWPC (two 896×640 mm^2 and two 1024×640 mm^2) were behind the carbon target. The analyzing target was made using an arrangement of 2-cm or 3-cm-thick graphite plates: 5 cm or 7 cm thicknesses were used depending on the turntable position

"A" or "B", respectively. The transverse polarization of the protons was measured via the azimuthal distribution of this second scattering on the carbon target. Each chamber consisted of two orthogonal sense planes, X and Y, using 20 μm tungsten wires with 2 mm wire spacing. The distance between the sense plane and the high voltage plane was 6 mm. All chambers were operated with the magic gas mixture [37].

2.4 Electronics and data acquisition

2.4.1 Electronics associated with PM's

The electronics for the neutron detector is described in [36]. Compact modules containing constant fraction discriminators (CFD) and mean-timers were developed and implemented in a double-width CAMAC unit. Each module could handle four neutron bars (8 PMs).

The trigger was constructed mainly with ECL electronics. This provided flexibility and computer control of the triggering conditions. All counters were connected to ADCs and TDCs. The radio frequency (RF) signal (50.63 MHz) of the accelerator was also recorded via a TDC for the measurement of the time-of-flight of the incident neutron (TOF_1).

2.4.2 Electronics associated with MWPCs and the second-level trigger

The preamplifiers, the encoding and the readout system used for the MWPCs are described in [38]. The main feature of the readout system is its plane-by-plane organization. In addition to the CAMAC readout, data were available on a separate connector suitable for a hardware fast decision logic. These data were the coordinate of the first encoded cluster and two bits indicating the track multiplicity in the plane.

A second-level trigger was needed for the polarimeter since only a small fraction ($\sim 5\%$) of the recoil protons scatter in the carbon analyzing target. The logical organization of the decision process is shown in Fig. 6. The data from the encoding system were sent into 3-input (4-input) "multiplexor-subtractors" (MPX3/MPX4). These modules chose the optimum two coordinates among the 3(4) planes of each telescope and computed the slopes of the trajectories. A NIM signal was provided when this calculation was not possible or ambiguous (R3 to R6). This allowed rejection of events with no particle in the telescopes or multiple track events. The calculation was still possible in cases where good events had one (two) planes with inefficiencies or parasite hits. For each x or y projection, the slopes of the incident and final trajectories were subtracted in "comparator-subtractor" modules (CS) to obtain an approximation of the projected scattering angles, $\tan(\theta_x)$ and $\tan(\theta_y)$. An additional module (MUL) then computed $\tan^2\theta_C = \tan^2\theta_x + \tan^2\theta_y$ which was sent into a final CS module which compared it with two programmable limits. A NIM signal was generated when $\tan^2\theta_C$ was outside of the limits (R7), allowing rejection of events without proper scattering in the carbon. We accepted events with a scattering angle between 3° and 30°. The final decision was taken by a module which collected the various NIM rejection signals. Activation of the rejections was programmable. In case of a rejection, a "fast clear" signal was sent to the various data acquisition modules (ADCs, TDCs, Registers, MWPC readout). The whole decision process to reject an event took less than 3 μsec.

2.4.3 Data acquisition

For the data acquisition, we used the TANDEM [39] system provided by PSI. It is based on an ACC2180 "starburst" front-end from CES communicating via ETHERNET with a DEC VAXstation. The front-end has access to the CAMAC branches using the "system crate". It reads the data which are then transferred to the VAXstation and written on EXABYTE tapes. Two other ACC2180s were used as auxiliary crate-controllers for compression of the data of the neutron counter and polarimeter. They also performed histogramming tasks for the control of the equipment. A PC which had access to the CAMAC via the system crate was used for downloading of the software into the two ACC2180 front-ends, for control of equipment parameters (e.g. triggering conditions and high voltages) and for histogram display.

2.4.4 Triggering and data taking conditions

For the calibration of the TOF and the ADC dependence of the S_{12} counter (calibrations are discussed in Sect. 3.3), we needed events with a well-defined time-of-flight. For that purpose we took data using the trigger "$M_3 \cdot S_{12}$" with the polarimeter platform at 0° and the lead filter removed from the beam. This gave us events with a well-defined TOF coming from photons produced in the neutron production target which converted into electrons in Monitor-1.

For the relative alignment of the MWPC we needed straight-track events in the polarimeter. These were obtained by taking data using the two arms in the "A" or "B" position without carbon plates in the polarimeter and triggering on "$\overline{M_3} \cdot S_{12} \cdot \overline{V_n} \cdot N_{or}$", where N_{or} is a simple OR of the neutron bars. The second-level trigger was activated in order to reject non-reconstructable trajectories in the polarimeter.

During the np elastic data taking, the first-level trigger was "$\overline{M_3} \cdot S_{12} \cdot \overline{V_n} \cdot N_{or}$" and the second-level trigger was enabled for the rejection of unscattered or non-reconstructible events. For each beam polarization, i.e every second, the trigger was changed for 10 ms to the calibration trigger "$M_3 \cdot S_{12}$" with no second-level rejection. This provided us with events suitable for the TOF offset calibration and allowed continuous monitoring of the time drifts of the phase of the accelerator RF.

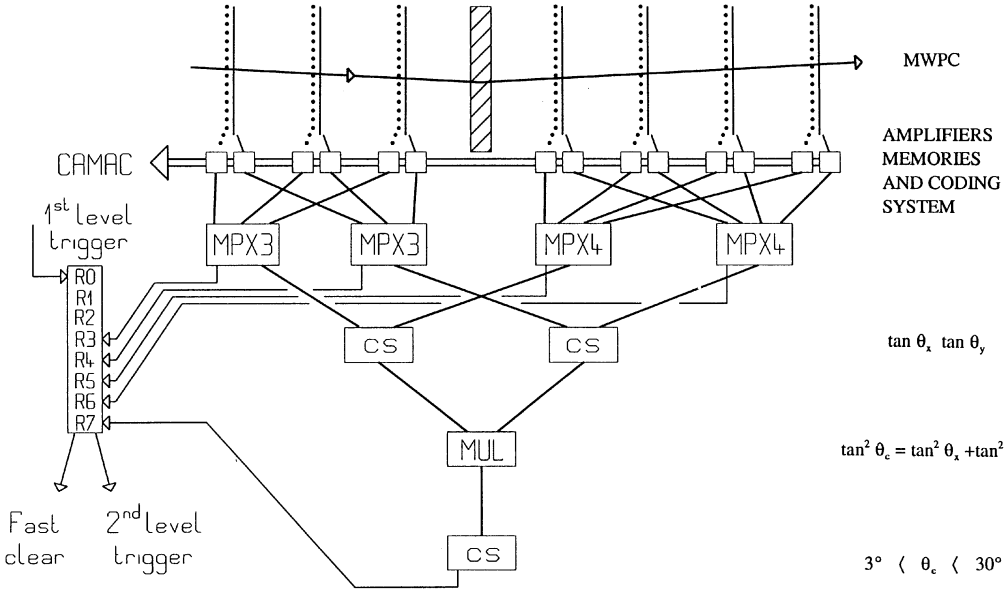

Fig. 6. A schematic representation of the hardware decision logic structure to select double-scattered events using information from the MWPCs

3 Data analysis

Besides the $\hat{s}, \hat{n}, \hat{k}$ reference frame as presented in Fig. 1, we also make use of the axes $(\hat{x}, \hat{y}, \hat{z})$ which refer to the fixed laboratory frame of the apparatus; $\hat{z}$ corresponds to the direction of the incident beam, $\hat{y}$ to the vertical upward direction and $\hat{x}$ to the sideway direction ($\hat{x} = \hat{y} \times \hat{z}$). Therefore $\hat{x}, \hat{y}, \hat{z}$ correspond to $\hat{s}, \hat{n}, \hat{k}$ at the center of the apparatus acceptance.

3.1 History of data acquisition

In order to measure the spin-transfer parameters $K_{os''so}$, K_{onno} and $K_{os''ko}$ it is necessary to carry out measurements with the three beam orientations $\hat{x}, \hat{y}, \hat{z}$. Roughly equal statistics were collected for each orientation. As the beam is not monochromatic and since the spin precession depends on the energy, the beam polarization for the $\hat{x}$ and $\hat{y}$ conditions has a parasitic component along the $\hat{z}$ direction. As far as possible we tried to record a well-balanced amount of data between the two different angular position "A" and "B" but unfortunately had no time to measure with the $\hat{s}$ beam in position "A". Therefore the $K_{os''so}$ parameter is available only in the c.m. angular region between 100^o and 160^o. Measurements of background were made using a dummy graphite target for each of the beam polarization orientation and angular settings.

3.2 General principle

The data analysis was carried out in two consecutive stages because of the large number of collected events ($\sim 1.3 \times 10^8$ raw events were written on tape during the data taking periods). In the first stage, the chamber and neutron data were converted to spatial coordinates and a rapid, loose selection of good event candidates was made for which both the reconstructed and raw informations were written onto data summary tapes (DST). The second stage of the analysis involved calculation of kinematical quantities on which cuts were applied, leading to the final sample of 'good' events. All these 'good' events were then used in the final calculation of the spin-dependent parameters as discussed in Sect. 4.

3.3 Preliminary calibrations

Before starting any reconstruction, several calibrations had to be performed.

3.3.1 General TOF offset

The energy of the incident neutron is determined from the relative timing between the S_{12} counter and a signal derived from the cyclotron RF system. Due to occasional changes of the parameters in the cyclotron during routine operation, fluctuations of the arrival time of the proton bunches at the neutron production target relative to the RF signal were observed. To monitor these fluctuations, events with a well-defined TOF were required. Once per second, the normal acquisition trigger was changed to the "calibration trigger - $M_3 \cdot S_{12}$" for 10 ms (see Sect. 2.4.4). Energetic photons from the production target undergo pair conversion in the lead of Monitor-1 and occasionally a fast ($v = c$) conversion electron/positron was detected in counter S_{12}, allowing measurement of the time-of-flight (TOF_γ) between the neutron production target and the S_{12} counter over a distance of 14.235 m. The general TOF offset (GTO) was taken as the difference between this measurement (TOF_γ) and the calculated TOF. During the first stage of the analysis the mean position of the TOF_γ peak was calculated from these calibration events in 15 minute intervals, thus allowing for correction of the GTO

during the second step of the analysis when the summary tapes were read again to extract the physical parameters.

Since the counter S_{12} was used for time-of-flight measurements, it was essential to work with a signal having a jitter as small as possible, to improve the energy resolution. We therefore corrected the S_{12} TDC signal for its amplitude dependence: this effect was anticipated as we did not use CFD discriminators. After corrections, the TOF_γ had a FWHM of $\sim$ 1 ns, mainly due to the phase acceptance of the accelerator. This led to an energy resolution on the quasi-elastic peak position of 40 MeV at 530 MeV and of 8 MeV at 250 MeV.

3.3.2 Offsets of the neutron bars

Each bar had a different horizontal central position and TOF offsets which could be determined using two thin vertical counters, T_1 and T_2, carefully positioned one meter apart just behind the neutron bars. By selecting events with a signal in a given neutron bar in coincidence with one of the T counters, a sample of events was obtained for which the horizontal and vertical impact points in the neutron counter were known. Only these events were used in the offset determination. They allowed the relation between the horizontal position and the timing difference between the two PMs to be calculated separately for each bar. In this calculation, an effective light velocity in the scintillator material of 15.5 cm/ns was used, the value measured with these bars in a low energy antiproton experiment at LEAR [36]. The central position offsets were determined to $\pm$ 3.0 mm.

For the TOF offsets, all the bars were adjusted with respect to the central bar (number six). This adjustment was done for each bar separately in the following way: the timing offset between a given horizontal bar and the two vertical timing counters T_1 and T_2 was found, these offsets were subtracted from that of bar number six, giving the relative offset between a given bar and bar number six. These two differences were then combined in a weighted mean taking into account the width of the peaks and the number of events. These TOF offsets are known to a precision of $\approx$ 70 ps.

3.3.3 Alignments of the MWPCs

In determining the precise spatial location of the MWPCs, it was assumed that construction errors were negligible compared to uncertainties in positioning them on the turntable. Since there are five degrees of freedom in specifing a location and orientation of a plane (one transverse displacement Δ_x or Δ_y depending on whether one has an x or y coordinate plane, one translation displacement along the $\hat{z}$ axis (Δ_z) and three rotational displacements around the reference axes ϕ_x, ϕ_y and ϕ_z), five parameters have to be determined for each plane, except for two planes in each x or y projection which act as references. Special data were collected without the carbon scatterer installed in the polarimeter allowing straight track events to be collected. From events having one and only one wire hit in all the 14 planes, it is possible to extract the five parameters for each plane. As one is working with small misalignments, it is possible to linearise the system of equations. Events with large slopes guarantee a good determination of parameters, such as Δ_z, which appear in the equations multiplied by the slope of the tracks.

3.4 Track reconstruction in MWPCs

After decoding the chamber data into individual hit wires for each plane, the horizontal and vertical slopes of the tracks upstream and downstream of the carbon target were reconstructed. The individual wire coordinates were first corrected for the transverse displacement (Δ_x or Δ_y) from which a first estimate of the trajectory's slope was computed. This allowed further correction for all the slope-dependent displacements. Due to the hardware decision logic, the topology of events for each coordinate (x or y) in the first telescope (containing three MWPC) consisted of exactly one hit per plane, or two planes with one hit and the third plane with either zero or more than one hits. In the multiple-hit case, the wire providing the best line fit was selected. Events for which the deviation from linearity was $\geq$ 2.5 mm ($\sim$ 0.2%) were rejected. From the slopes, the proton trajectory $\hat{k}''$ was determined and the proton polar and azimuthal angles θ_p and ϕ_p calculated.

For the backward telescope containing four MWPCs, the hardware decision logic provided events having at least two X and two Y planes with a single hit, the two remaining planes also had no-hit or multiple-hit possibilities. All possible track combinations were considered and the one giving the best χ^2 was kept. Once the trajectories on both sides of the carbon had been reconstructed, the scattering angle θ_C and the azimuthal angle ϕ_C in the carbon were computed from

$$\begin{aligned} \cos\theta_C &= \hat{k}'' \cdot \hat{k}_C \\ \cos\phi_C &= \hat{n} \cdot \hat{n}_C \\ \sin\phi_C &= -\hat{s}'' \cdot \hat{n}_C \end{aligned} \tag{7}$$

where $\hat{n}$ and $\hat{n}_C$ are the normals to the plane of the np and pC scattering, respectively

$$\hat{n} = \frac{\hat{k} \times \hat{k}'}{|\hat{k} \times \hat{k}'|} \equiv -\frac{\hat{k} \times \hat{k}''}{|\hat{k} \times \hat{k}''|}, \qquad \hat{n}_C = \frac{\hat{k}'' \times \hat{k}_C}{|\hat{k}'' \times \hat{k}_C|}. \tag{8}$$

Here $\hat{k}_C$ is along the direction of the scattered particle after the rescattering and $\hat{k}'$ represents the scattered neutron trajectory as shown in Fig. 1. Finally the square of the minimum distance between the incoming and outgoing proton trajectories was calculated (d^2_{min}) as well as the longitudinal vertex position (Z_C). Figure 7a shows the vertex position Z_C and Fig. 7b the reconstructed scattering angle θ_C. In Fig. 7b the hardware cut which rejected events with scattering angles smaller than 3° is

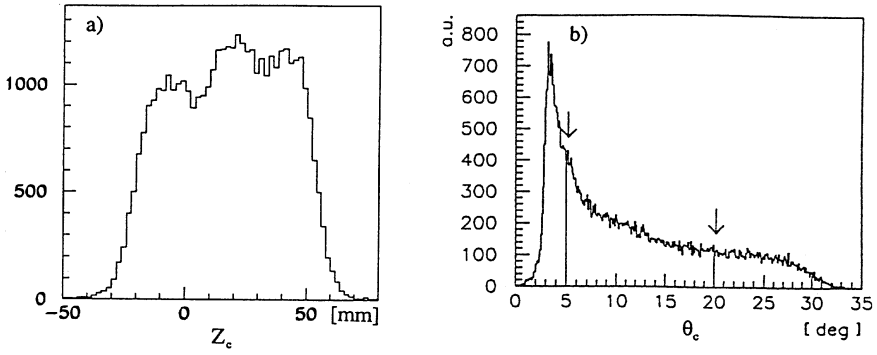

Fig. 7. Reconstructed variables relevant to the proton polarimeter: **a** the longitudinal vertex in the Carbon, Z_C, **b** the scattering angle θ_C. The hardware decision logic causes the rapid drop below 3°. The *arrows* indicate where the cuts were made in the analysis

seen. Those events do not contribute any useful information as the carbon analyzing power A_C drops rapidly to zero for small scattering angles. Cuts were applied on these reconstructed quantities as illustrated by the arrows in Fig. 7.

3.5 Neutron position reconstruction

The vertical position of the neutron interaction was determined from the knowledge of which bar was hit. Events with signals in multiple bars were rejected. The time difference between the PMT signals provided the neutron horizontal position coordinate. The horizontal position resolution for charged particles had a FWHM of about 5.8 cm. It is estimated that the resolution is slightly worse for neutrons. The vertical FWHM was taken as a bar height (8 cm). The time sum from the neutron bar PMTs, combined with a corrected start signal from the proton TOF start signal, determined the neutron TOF. The slope of the neutron trajectory was then calculated using the X and Y impact point in a bar and the center of the CH_2 target as coordinates. As for the proton trajectory, the neutron trajectory $\hat{k}'$ was determined and the neutron scattering angle θ_n and azimuthal angle ϕ_n were calculated.

3.6 Determination of the incident neutron energy

Since the neutron beam was not monoenergetic, it was necessary to calculate the incident neutron kinetic energy T_o (or β_o) on an event-by-event basis. This could be extracted from the measurement of the time-of-flight between the neutron production target and the counter S_{12} (TOF_1). The incident neutron travelled a distance L_o between the production target and the CH_2 target. After the scattering, the scattered proton travelled a distance L_p (0.5 m) up to the S_{12} counter. Since we had no direct measurement of the velocity of the proton, it was calculated iteratively (using θ_{pt}, the proton angle in its telescope) starting from the value

$$\beta_o = \frac{L_o + L_p/\cos\theta_{pt}}{c \times TOF_1}. \qquad (9)$$

The iterative procedure contained three steps

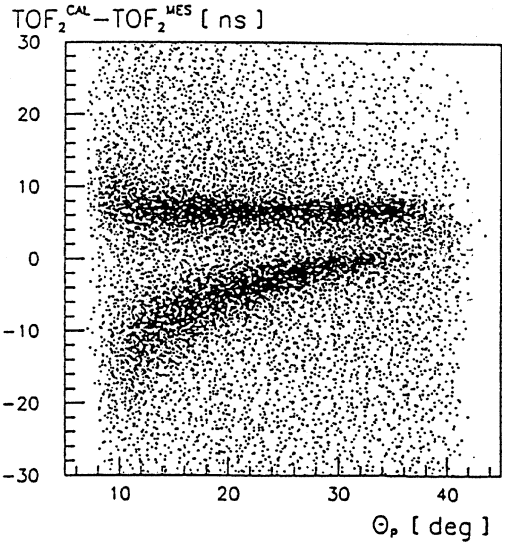

Fig. 8. Scatter plot of the difference between the calculated and measured time-of-flight ($TOF_2^{cal} - TOF_2^{mes}$) versus the laboratory proton angle θ_p. The incident neutrons to which the wrong micro-burst was assigned show up in the curved band. The good events are in the horizontal band (see text)

1. calculation of the c.m. scattering angle $\theta^\star$ as a weighted average of the c.m. angles calculated from the proton ($\theta_p^\star$) and neutron ($\theta_n^\star$) measurement separately. The weights were given by the angular resolutions. The azimuthal angle of the scattering plane ϕ has been calculated in a similar way from ϕ_n and ϕ_p.
2. calculation of the proton kinetic energy T_p from β_o and $\theta^\star$ taking into account the energy loss of the proton between the CH_2 vertex and the counter S_{12}.
3. correct β_o calculation using the effective recoil proton kinetic energy found previously. The iteration stopped when the change in the incident neutron kinetic energy was less than 0.1 MeV.

There is an ambiguity in the energy determination. At a distance of 13.735 m a fast neutron and a slow neutron coming from a preceeding micro-burst arriving 19.75 ns earlier (see Sect. 2.1) cannot be distinguished. To resolve this ambiguity, we made use of a second TOF information, namely the time-of-flight difference between the neutron and the proton, TOF_2^{mes}. This quantity can also be calculated, TOF_2^{cal}, up to an overall offset from the infor-

mation obtained on the kinematics of the reaction in the preceeding iterative calculation. Figure 8 shows a scatter plot of the difference ($\Delta\mathrm{TOF}_2 = \mathrm{TOF}_2^{cal} - \mathrm{TOF}_2^{mes}$) versus the proton angle θ_p for data taken in position "B". One clearly identifies two bands, a horizontal band corresponding to the good events and a curved band containing events for which the neutrons actually came from the preceeding micro-burst. For data taken in position "A", the second band is less visible since protons at large recoil angle θ_p had insufficient energy to go through the carbon analyser in the polarimeter. The angular dependence is understood and can easily be calculated. The distance between the two bands is independent of the incident kinetic energy and inversely proportional to sin θ_p. A cut was applied on the 2-dimensional plot to select the good events.

3.7 Kinematical cuts

In order to select elastic events, cuts have been applied on the opening angle and coplanarity. Figure 9a shows the difference $\Delta\phi$ ($\equiv \phi_n - \phi_p$) between the ϕ angles calculated for the neutron and proton. The distribution is centered around 180°. Figure 9b shows the difference in the c.m. neutron scattering angle calculated either from the neutron information or the proton information, $\theta_n^\star - \theta_p^\star = \Delta\theta^\star$. In the final analysis, we have applied cuts on these two quantities at the $\pm 3\sigma$ level. The shaded area in Figs. 9a and 9b show one distribution after cutting on the other one and on ΔTOF_2.

3.8 Background subtraction

For the background subtraction, data were taken with the cylindrical CH_2 target replaced by a carbon target. These data were analyzed with the same off-line reconstruction program and cuts as used for the CH_2 target. The fraction of the background, f_b, to be subtracted from the CH_2 data is given by

$$f_b = \frac{M_C^A}{M_{CH_2}^A}\,\frac{\rho_{CH_2}}{\rho_C}\,\frac{V_{CH_2}}{V_C}\,\frac{B_{CH_2}}{B_C} \;\approx\; 0.5\,\frac{B_{CH_2}}{B_C} \qquad (10)$$

where B_{CH_2} and B_C are the integrated beam intensities for the CH_2 and C target data, ρ_{CH_2} and $M_{CH_2}^A$ are the CH_2 density and atomic number respectively (similar quantities are defined for the carbon data). V_{CH_2} and V_C are the intersection volumes between the beam and the corresponding target. In order to check that this factor was properly calculated, CH_2 and C data were analyzed with no kinematical cut. The difference in the c.m. neutron scattering angle calculated either from the neutron or the proton information, $\Delta\theta^\star$, is shown in Fig. 10 separately for the two types of data. The tails of the two distributions overlap nicely. The asymmetry in the background distribution is due to the fact that the (n,np) Q-value results in an available energy that is always smaller than that available for elastic np scattering. Therefore, one observes a decrease of the opening angle between the proton and the neutron. This shrinking of the opening angle manifests itself as negative values in $\Delta\theta^\star$. After all the cuts were made, the fraction of the background in our data was $\sim 1.5\%$ for the position "B" and $\sim 5\%$ for the position "A".

4 Estimators for the spin-dependent parameters

The choice of the statistical estimators used to extract the observables A_{oono}, K_{onno}, $K_{os''ko}$ and $K_{os''so}$ depends on the experimental conditions. For our measurement with a CH_2 target and a polarized beam which was flipped every second, we have used estimators requiring the same detection efficiency of our experimental apparatus (η) for the two beam polarization states. Note that this class of estimators is not appropriate for measurements with a polarized target for which the spin is reversed only every two to three days: for infrequent spin reversals, one has to use estimators requiring identical acceptance and detection efficiencies for particles scattered to the left and to the right in the polarimeter. Such estimators could also be used here, but are less suitable since they lead to a smaller sample of selected good events because of the more stringent efficiency/acceptance conditions.

For each kinetic energy bin T_o and each c.m. angular $\theta^\star$ bin in the np scattering, the expected number $N^\pm(\phi,\theta_C,\phi_C)$ of accepted events for each of the two beam polarization orientations (+ or −) is given by

$$\begin{aligned} N^\pm(\phi,\theta_C,\phi_C) = {} & B^\pm\ \eta\ I_{o1}\ I_{o2} \\ & \times(1 + P_{bn}^\pm A_{oono} + P_{onoo} A_C(T_p,\theta_C)\cos\phi_C \\ & + K_{onno} A_C(T_p,\theta_C) P_{bn}^\pm \cos\phi_C \\ & - K_{os''so} A_C(T_p,\theta_C) P_{bs}^\pm \sin\phi_C \\ & - K_{os''ko} A_C(T_p,\theta_C) P_{bk}^\pm \sin\phi_C). \end{aligned} \qquad (11)$$

Here $B^\pm$ are the integrated beam intensities for the two beam orientations, η the detection efficiency (which is identical for the two spin orientations); I_{o1}, I_{o2} are the unpolarized differential cross sections for the first (np) and second (pC) scattering; $A_C(T_p,\theta_C)$ is the effective proton-carbon analyzing power which depends on the scattered proton kinetic energy T_p and on the scattering angle θ_C. $P_{bs}^\pm$, $P_{bn}^\pm$ and $P_{bk}^\pm$ are the beam polarization components in the $\hat{s},\hat{n},\hat{k}$ reference frame; the $(-)$ components have an opposite intrinsic sign from the $(+)$ components. These quantities can be calculated from the laboratory components $P_{bx}^\pm$, $P_{by}^\pm$ and $P_{bz}^\pm$ by applying a rotation ϕ about the $\hat{z}$ ($\equiv \hat{k}$ axis) axis.

For a given $\theta^\star$, the detection efficiency function η can be eliminated by introducing an asymmetry ϵ_i, defined for each angular bin i in ϕ,θ_C,ϕ_C:

$$\epsilon_i = \frac{(1-\gamma)N_i^+ - (1+\gamma)N_i^-}{|P_b^-|(1-\gamma)N_i^+ + |P_b^+|(1+\gamma)N_i^-}\,, \qquad (12)$$

where $\gamma = \frac{B^+ - B^-}{B^+ + B^-}$ is the asymmetry in the integrated beam intensity for the two beam polarization states. In-

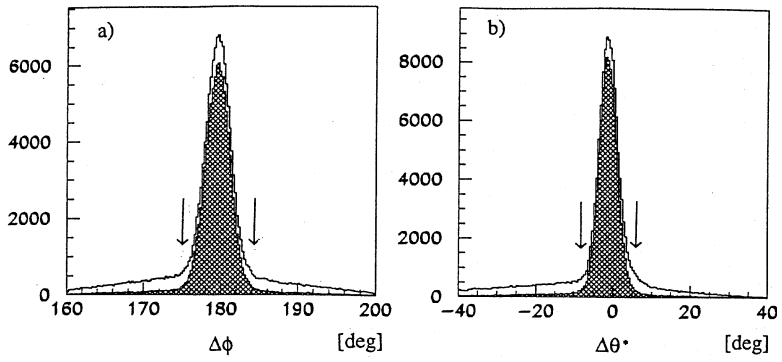

Fig. 9. a Difference in azimuthal angles ($\Delta\phi \equiv \phi_n - \phi_p$) calculated from the neutron and proton information (coplanarity test). **b** Difference $\Delta\theta^\star$ calculated from the neutron and proton information. The *empty histogram* corresponds to the raw data. The *filled histogram* shows one distribution after cuts on ΔTOF_2 as well as cuts on the other distribution. *Arrows* indicate where the cuts were placed

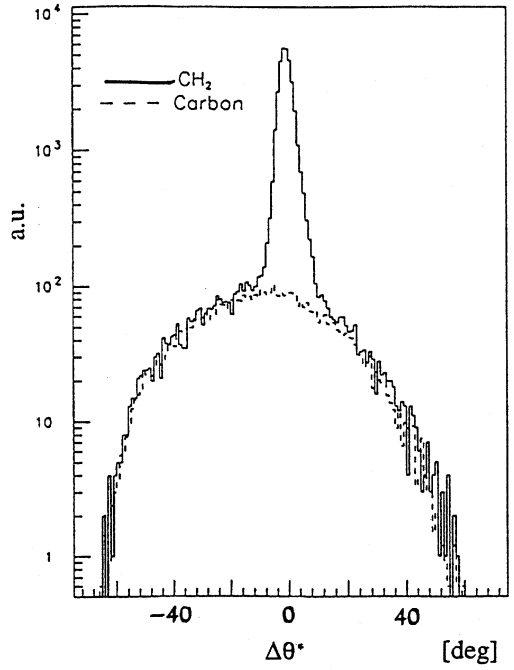

Fig. 10. Difference $\Delta\theta^\star$ calculated from the neutron and proton information. The *full line* is obtained with the CH_2 data and the *dashed line* with the carbon data after proper normalization

troducing (11) into (12), one obtains

$$\epsilon_i = \frac{1}{P_b\,\Delta}(P_{bn}\,A_{oono} + K_{onno}\,P_{bn}\,A_C\cos\phi_C - K_{os''so}\,P_{bs}\,A_C\sin\phi_C - K_{os''ko}\,P_{bk}\,A_C\sin\phi_C). \quad (13)$$

Here $\Delta = 1 + P_{onoo}\,A_C\,cos\phi_C$ and $P_b = \frac{1}{2}[P_b^+ - P_b^-]$ is the mean beam polarization (similarly for P_{bs}, P_{bn} and P_{bk}). The quantity Δ can be calculated taking $P_{onoo} \equiv A_{oono}$ values obtained from a phase shift analysis [27] and using a previous parametrization of A_C which we developed for our polarimeter calibration measurements [40].

The asymmetry ϵ_i can be written as a linear combination of the four spin parameters A_{oono}, K_{onno}, $K_{os''ko}$ and $K_{os''so}$ ($\equiv C_\alpha$, α= 1,...4)

$$\epsilon_i = \sum_\alpha f_{i\alpha} C_\alpha \quad (14)$$

Table 1. Position "A" values for A_{oono} , K_{onno} and $K_{os''so}$ for *np* elastic scattering at incident neutron beam energies (T_o) 260, 318, 386, 472 and 538 MeV. The quoted errors are statistical, for systematic ones see Table 3

T_o	$\theta^\star$	A_{oono}		K_{onno}		$K_{os''ko}$	
[MeV]	[deg]	value	error	value	error	value	error
	104.4	-0.247	0.048	0.249	0.192	0.220	0.117
260	112.3	-0.230	0.036	-0.048	0.125	0.258	0.089
	118.0	-0.242	0.063	-0.588	0.200	0.253	0.170
	89.2	-0.177	0.054	0.020	0.245	0.130	0.118
318	96.4	-0.167	0.032	0.148	0.114	0.183	0.083
	104.2	-0.284	0.033	-0.117	0.097	0.418	0.070
	112.1	-0.159	0.032	-0.027	0.087	0.324	0.060
	118.1	-0.208	0.050	-0.304	0.135	0.217	0.103
	80.7	-0.189	0.033	-0.060	0.132	0.252	0.084
386	88.1	-0.204	0.026	0.084	0.086	0.259	0.064
	96.0	-0.232	0.028	-0.066	0.079	0.270	0.058
	104.0	-0.285	0.029	-0.164	0.077	0.339	0.055
	112.1	-0.227	0.028	-0.263	0.075	0.381	0.053
	118.0	-0.209	0.040	-0.183	0.114	0.275	0.084
	73.0	-0.003	0.030	0.052	0.120	0.016	0.079
	80.2	-0.194	0.029	0.148	0.086	0.181	0.065
472	87.9	-0.250	0.032	0.023	0.088	0.080	0.063
	96.0	-0.313	0.032	-0.028	0.088	0.268	0.064
	104.0	-0.325	0.033	-0.038	0.095	0.320	0.067
	112.0	-0.251	0.031	-0.224	0.096	0.448	0.068
	118.0	-0.219	0.048	-0.297	0.157	0.419	0.115
	65.9	0.076	0.030	-0.062	0.127	-0.080	0.074
	72.0	-0.019	0.020	-0.124	0.064	0.052	0.050
	80.0	-0.129	0.024	-0.098	0.064	0.142	0.050
538	87.9	-0.207	0.025	0.175	0.068	0.184	0.051
	96.0	-0.251	0.025	0.035	0.074	0.278	0.055
	103.8	-0.320	0.025	0.081	0.080	0.291	0.060
	111.8	-0.306	0.025	-0.089	0.085	0.295	0.065
	118.0	-0.315	0.043	-0.213	0.158	0.351	0.130

where the $f_{i\alpha}$ are

$$f_{i1} = \frac{1}{\Delta}\frac{P_{bn}}{P_b} = \frac{1}{\Delta}(\cos\phi\frac{P_{by}}{P_b} - \sin\phi\frac{P_{bx}}{P_b})$$

$$f_{i2} = \frac{1}{\Delta}\frac{P_{bn}}{P_b}A_C\cos\phi_C = \frac{1}{\Delta}(\cos\phi\frac{P_{by}}{P_b} - \sin\phi\frac{P_{bx}}{P_b})A_C\cos\phi_C$$

Table 2. Position "B" values for A_{oono}, K_{onno}, $K_{os''so}$ and $K_{os''ko}$ for np elastic scattering at incident neutron beam energies (T_o) 260, 318, 386, 472 and 538 MeV. The quoted errors are statistical, for systematic ones see Table 3

T_o	$\theta^\star$	A_{oono}		K_{onno}		$K_{os''ko}$		$K_{os''so}$	
[MeV]	[deg]	value	error	value	error	value	error	value	error
	105.4	-0.201	0.048	-0.143	0.173	0.398	0.196	0.362	0.215
	112.5	-0.127	0.025	-0.149	0.082	0.265	0.091	-0.166	0.098
	120.2	-0.200	0.020	-0.129	0.059	0.015	0.066	0.010	0.070
	128.1	-0.157	0.019	-0.099	0.050	0.018	0.054	-0.219	0.059
260	136.1	-0.127	0.018	-0.057	0.046	-0.053	0.048	-0.430	0.053
	144.0	-0.127	0.017	0.034	0.046	-0.038	0.047	-0.655	0.052
	151.9	-0.110	0.020	0.015	0.052	-0.220	0.055	-0.655	0.060
	159.0	-0.096	0.028	0.085	0.074	-0.228	0.086	-0.764	0.092
	105.1	-0.183	0.023	-0.199	0.065	0.277	0.081	0.150	0.081
	112.2	-0.198	0.018	-0.117	0.047	0.330	0.057	0.027	0.054
	120.1	-0.176	0.016	-0.107	0.042	0.221	0.048	-0.069	0.047
	128.1	-0.172	0.014	-0.073	0.038	0.078	0.042	-0.204	0.043
318	136.1	-0.143	0.013	-0.068	0.035	-0.007	0.037	-0.382	0.039
	144.0	-0.117	0.012	0.038	0.034	-0.054	0.035	-0.500	0.038
	151.8	-0.105	0.014	0.090	0.038	-0.168	0.041	-0.728	0.043
	159.0	-0.074	0.019	0.201	0.055	-0.152	0.062	-0.806	0.066
	105.4	-0.265	0.021	-0.106	.055	0.398	0.073	0.204	0.066
	112.0	-0.237	0.015	-0.236	0.039	0.323	0.048	0.168	0.043
	120.0	-0.205	0.013	-0.204	0.037	0.329	0.045	0.021	0.041
	128.0	-0.157	0.012	-0.148	0.034	0.118	0.039	-0.143	0.038
386	136.0	-0.145	0.010	-0.096	0.031	0.077	0.034	-0.269	0.034
	144.1	-0.101	0.009	0.022	0.030	-0.031	0.031	-0.430	0.032
	151.8	-0.107	0.010	0.175	0.032	-0.125	0.035	-0.634	0.035
	159.0	-0.095	0.014	0.364	0.047	-0.184	0.054	-0.808	0.055
	105.5	-0.351	0.026	-0.095	0.074	0.624	0.108	0.001	0.086
	111.8	-0.303	0.016	-0.194	0.047	0.440	0.064	0.165	0.051
	120.0	-0.246	0.014	-0.215	0.046	0.343	0.058	0.155	0.051
	128.1	-0.196	0.012	-0.137	0.044	0.274	0.053	0.091	0.048
472	136.1	-0.143	0.011	-0.041	0.040	0.069	0.047	-0.135	0.043
	144.0	-0.102	0.010	0.059	0.037	0.091	0.041	-0.343	0.039
	151.9	-0.089	0.009	0.188	0.037	-0.064	0.042	-0.555	0.041
	158.9	-0.062	0.013	0.204	0.056	-0.121	0.068	-0.660	0.065
	105.6	-0.278	0.025	0.021	0.079	0.403	0.115	0.207	0.092
	112.0	-0.276	0.013	-0.108	0.045	0.265	0.057	0.043	0.048
	120.0	-0.269	0.013	-0.129	0.046	0.311	0.058	0.161	0.050
	128.0	-0.193	0.011	-0.141	0.043	0.266	0.054	0.072	0.047
538	136.0	-0.140	0.010	-0.074	0.040	0.204	0.046	-0.027	0.042
	144.0	-0.095	0.009	0.001	0.036	0.117	0.040	-0.212	0.038
	151.9	-0.058	0.008	0.195	0.036	-0.022	0.041	-0.376	0.039
	158.8	-0.038	0.012	0.400	0.054	-0.038	0.068	-0.638	0.063

$$
\begin{aligned}
f_{i3} &= \frac{-1}{\Delta}\frac{P_{bs}}{P_b}A_C\sin\phi_C \\
&= \frac{-1}{\Delta}(\sin\phi\frac{P_{by}}{P_b} + \cos\phi\frac{P_{bx}}{P_b})A_C\sin\phi_C \\
f_{i4} &= \frac{-1}{\Delta}\frac{P_{bk}}{P_b}A_C\sin\phi_C = \frac{-1}{\Delta}\frac{P_{bz}}{P_b}A_C\sin\phi_C\,. \qquad (15)
\end{aligned}
$$

In matrix notation, (14) becomes $\tilde{\epsilon} = \tilde{f}\tilde{C}$ (the $\tilde{}$ sign indicates matrices). It is then possible to extract the four spin parameters by using a linear least-square fit method [41]. One finds

$$\tilde{C} = (\tilde{f}^T\tilde{\omega}\tilde{f})^{-1}\,(\tilde{f}^T\tilde{\omega}\tilde{\epsilon}) \equiv \tilde{A}^{-1}\tilde{B}\,. \qquad (16)$$

where $\tilde{\omega}$ is the weight matrix (inverse of the covariance matrix) for the experimental measurements. In this notation $\tilde{A}^{-1}$ is the covariance matrix for the four spin parameters.

The elements of the [4×4] matrix $\tilde{A}$ and of the [4×1] $\tilde{B}$ matrix are defined as

$$A_{\alpha\beta} = \sum_{bin\,i}\omega_i\,f_{i\alpha}f_{i\beta}$$

$$B_\alpha = \sum_{bin\,i}\omega_i\,\epsilon_i\,f_{i\alpha} \qquad (17)$$

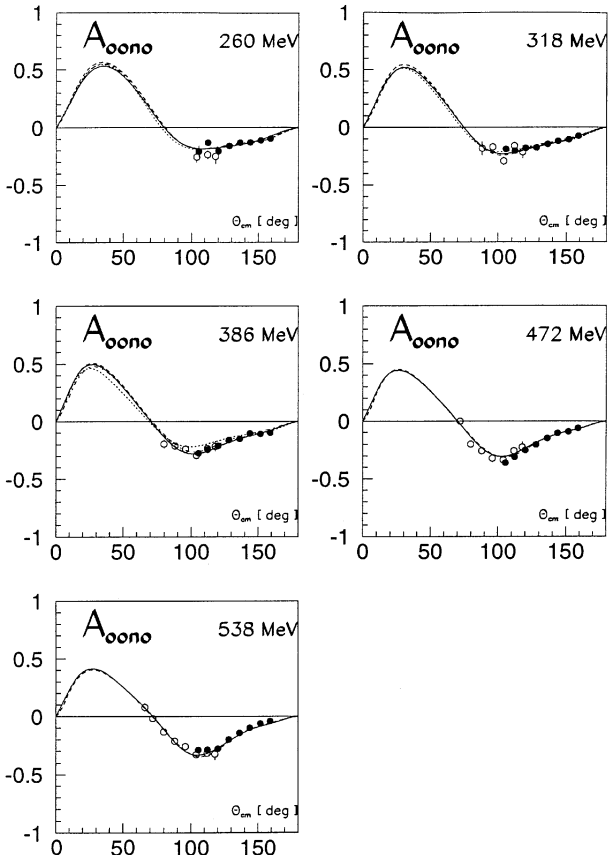

Fig. 11. Results for the A_{oono} parameter at the 260, 318, 386, 472 and 538 MeV shown as *open circles* for position "A" and *black dots* for position "B". The *full* and *dashed lines* are PSA predictions [26,27] respectively. The *dotted* and *dashed-dotted lines* are potential model predictions [28,29] respectively

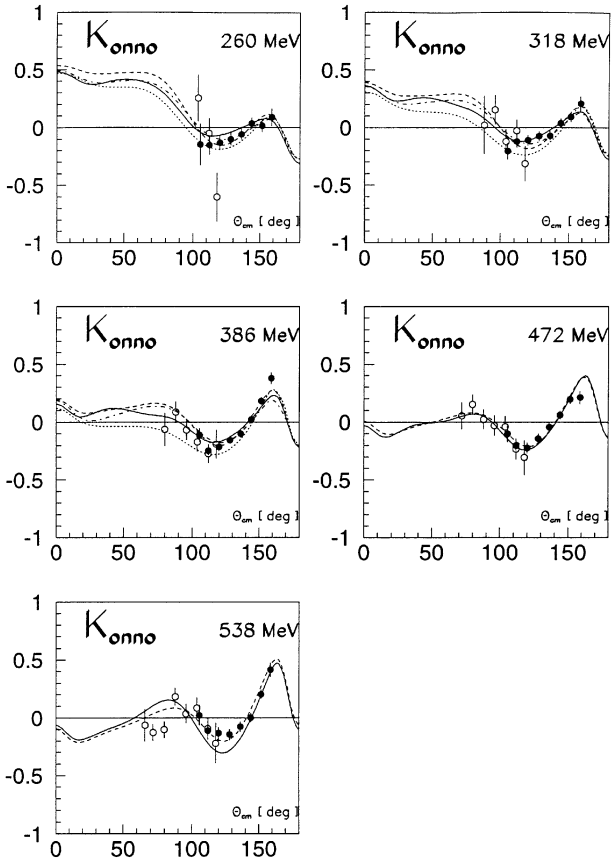

Fig. 12. Results for the K_{onno} parameter at 260, 318, 386, 472 and 538 MeV shown as *open circles* for position "A" and *black dots* for position "B". The *full* and *dashed lines* are PSA predictions [26,27] respectively. The *dotted* and *dashed-dotted lines* are potential model predictions [28,29] respectively

A first order approximation of the weight ω_i is

$$\omega_i = \frac{1}{\sigma_{\epsilon i}^2} \approx P_b[|P_b^-|(1-\gamma)N_i^+ + |P_b^+|(1+\gamma)N_i^-]\,. \quad (18)$$

By introducing (18) into (17), one finds the important property that the sums over the ϕ, θ_C, ϕ_C angular bins weighted by ω_i can be replaced by sums over the events with a weight equal to one. The matrices $\tilde{A}$ and $\tilde{B}$ are then given by

$$\begin{aligned} A_{\alpha\beta} &= P_b\,|P_b^-|(1-\gamma) \sum_{events+} f_\alpha f_\beta \\ &\quad + P_b\,|P_b^+|(1+\gamma) \sum_{events-} f_\alpha f_\beta \\ B_\alpha &= P_b\,(1-\gamma) \sum_{events+} f_\alpha \\ &\quad - P_b\,(1+\gamma) \sum_{events-} f_\alpha . \end{aligned} \quad (19)$$

Here $\sum_{events+}$ and $\sum_{events-}$ represent the sums over the good events for the beam polarization (+) and (−), respectively. From (19) one notices that each term of either the $\tilde{A}$ or $\tilde{B}$ matrix is given by sums over events ($\sum_{events-}$ and $\sum_{events+}$) of terms like $\cos\phi \sin\phi \cos\phi_C$. In total, 30 such sums are computed for each $\theta^\star$ and T_o bin, including the two sums for the number of events $\sum_{events+}$ and $\sum_{events-}$.

To subtract background, the formalism must be modified. The same form as (19) has been retained but $A_{\alpha\beta}$ and B_α are redefined to incorporate measurements made with the dummy carbon target. Using the background fraction f_b defined by (10), we have

$$\begin{aligned} A_{\alpha\beta} &= A_{\alpha\beta}^{CH_2} - f_b\, A_{\alpha\beta}^{C} \\ B_\alpha &= B_\alpha^{CH_2} - f_b\, B_\alpha^{C} \\ Var(\tilde{B}) &= \tilde{A}^{CH_2} + f_b^2\, \tilde{A}^{C}\,. \end{aligned} \quad (20)$$

The spin observables are obtained from (16):

$$\tilde{C} = \tilde{A}^{-1}\, \tilde{B}$$

but when the background corrections is calculated $\tilde{A}^{-1}$ is no longer the covariance matrix. The errors are given by

$$Var(\tilde{C}) = \tilde{A}^{-1}(\tilde{A}^{CH_2} + f_b^2\, \tilde{A}^{C})\tilde{A}^{-1}$$

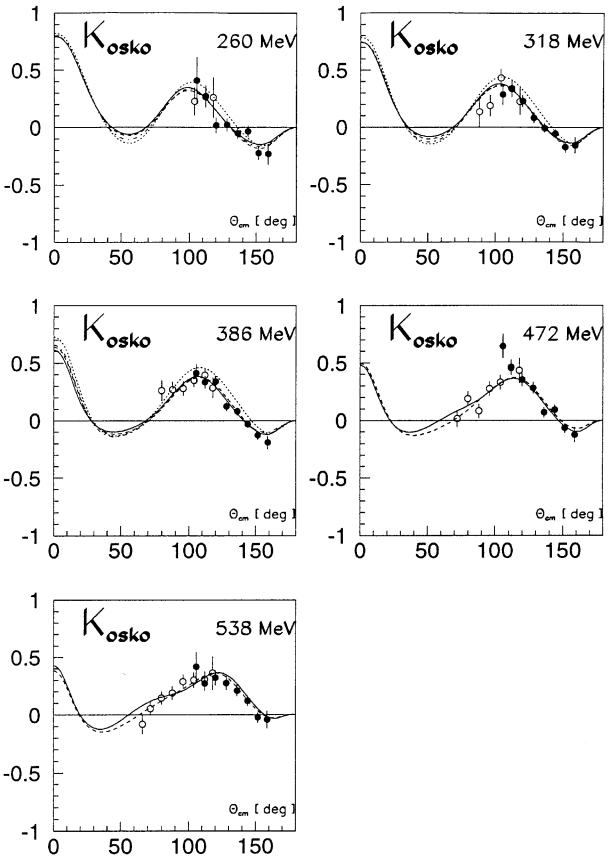

Fig. 13. Results for the $K_{os''ko}$ parameter at 260, 318, 386, 472 and 538 MeV shown as *open circles* for position "A" and *black dots* for position "B". The *full* and *dashed lines* are PSA predictions [26,27] respectively. The *dotted* and *dashed-dotted lines* are potential model predictions [28,29] respectively

$$Var(\tilde{C}) = (\tilde{A}^{CH_2} - f_b\,\tilde{A}^C)^{-1}(\tilde{A}^{CH_2} + f_b^2\,\tilde{A}^C) \times(\tilde{A}^{CH_2} - f_b\,\tilde{A}^C)^{-1}\,. \quad (21)$$

The data were divided into 18 bins of 20 MeV width for the incident kinetic energy between 230 and 590 MeV. The scattering angle ranges of positions "A" and "B" were each divided into 16 bins each 4° (c.m.) wide. As a consequence, there were 8640 sums to compute. Sums for data taken under the same beam and target conditions and turn-table settings were combined. For the final data presentation, the data were grouped to provide 8^o (c.m.) wide angular bins in five energy ranges which were chosen to have about equal statistics in each energy range.

5 Results and discussion

Results for the analyzing power, A_{oono}, as well as for the spin-dependent parameters $K_{onno}, K_{os''so}$ and $K_{os''ko}$ have been obtained for five incident kinetic energy ranges with mean energies 260, 318, 386, 472 and 538 MeV. Results were obtained in the c.m. ranges $64° - 124°$ (position "A") and $104^o - 164^o$ (position "B"). The 20^o overlap provided an internal consistency check of the data. $K_{os''so}$ data were only measured in position "B". The fraction of raw events kept in the final analysis represented 4.5% and 7% for the CH_2 data in positions "A" and "B", respectively. Similar numbers for the Carbon data gave 0.5% and 0.3%, respectively.

Table 3. Relative systematic errors in percent for the two-polarization transfer parameters. The multiplicative global effects of P_b and A_C are included

$\theta^\star$	260 MeV	318 MeV	386 MeV	472 MeV	538 MeV
64°					±7.2 %
72°				±5.9 %	±3.9 %
80°			±5.7 %	±3.8 %	±2.5 %
88°		±6.5 %	±3.9 %	±2.9 %	±2.5 %
96°	±8.4 %	±4.6 %	±2.6 %	±2.8 %	±2.5 %
104°	±6.4 %	±3.4 %	±2.4 %	±2.8 %	±2.5 %
112°	±4.9 %	±2.6 %	±2.4 %	±2.8 %	±2.5 %
120°	±4.0 %	±2.4 %	±2.4 %	±2.8 %	±2.5 %
128°	±3.3 %	±2.4 %	±2.4 %	±2.8 %	±2.5 %
136°	±3.4 %	±2.4 %	±2.4 %	±2.8 %	±2.5 %
144°	±2.8 %	±2.4 %	±2.4 %	±2.8 %	±2.5 %
152°	±2.8 %	±2.4 %	±2.4 %	±2.8 %	±2.5 %
160°	±2.8 %	±2.4 %	±2.4 %	±2.8 %	±2.5 %

Final results with their statistical errors are given in Table 1 (position "A") and Table 2 (position "B"). Figures 11 to 14 illustrate the energy dependence of each of the four measured spin parameters plotted as a function of the c.m. angle $\theta^\star$. Black dots denote position "B" and open circles are used for position "A". In the overlap region between 100° and 120° one observes an excellent agreement between the two data sets. For energies below 400 MeV these results are compared to the Paris [28] and Bonn [29] potential model predictions which are shown as dotted and dashed-dotted lines, respectively. The full and dashed lines are predictions from the Saclay-Geneva phase shift analysis [27] and the SAID program (solution FA95) [26], respectively, before introduction of these new data points. The Bonn potential model predictions are in relatively good agreement with the PSA. On the other hand, the Paris potential needs some ajustment. The agreement between the two PSA predictions is quite good at low energies but becomes worse at 538 MeV for all the two-spin parameters. This is due to a lack of data in this energy range.

Multiplicative and additive systematic errors will be discussed separately in the following. Multiplicative errors are due to uncertainties in the determination factors of the spin observables. Two terms contribute:

– The neutron beam polarization has been measured in a dedicated experiment [32]. Statistical errors of the calibration measurements are a source of common systematic errors. The beam polarization values used in the analysis have been calculated by fitting curves to the calibration data. The relative error, $\Delta P_B/P_B$, varies from 1.8 % to 3 % as a function of the neutron energy [32].

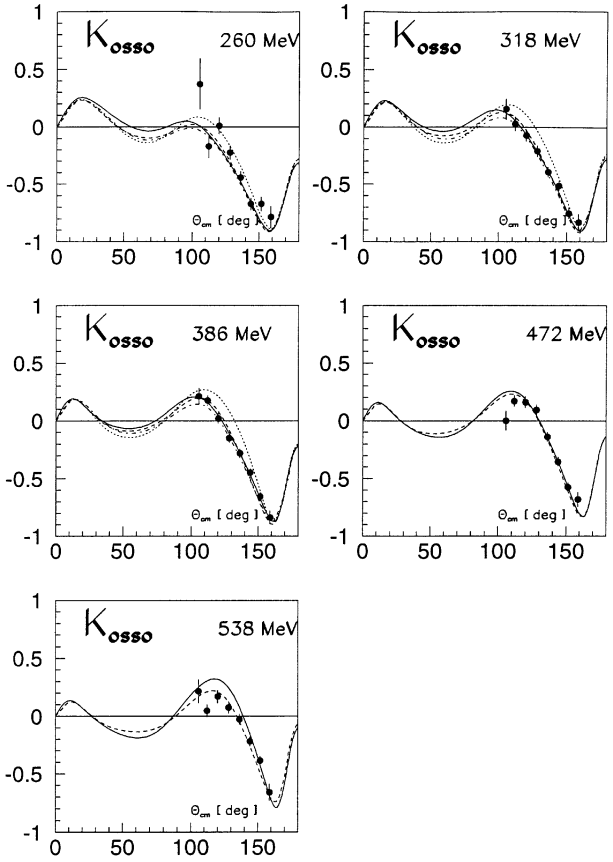

Fig. 14. Results for the $K_{os''so}$ parameter at 260, 318, 386, 472 and 538 MeV shown as *black dots* for position "B". The *full* and *dashed lines* are PSA predictions [26,27] respectively. The *dotted* and *dashed dotted lines* are potential model predictions [28,29] respectively

– The carbon analyzing power, A_C, has been measured [40] with an error dominated by the statistical precision and the proton beam polarization uncertainty, both contributing about 1%. At low energy the error is dominated by the uncertainty in the beam energy. However, the relative error $\Delta A_C/A_C$ is a function of the re-scattered proton energy. In order to link this uncertainty to our observables, the relative error has been expressed as a function of the c.m. scattering angle and the incident neutron beam energy. It was found to be almost constant (1.5%) except at low neutron energy and for small c.m. scattering angles (corresponding to large proton laboratory angles). In this region, the relative error increased rapidly up to $\sim 8\%$.

Adding the contributions from the beam polarization and carbon analyzing power uncertainties quadratically, the estimated relative systematic uncertainty for the polarization transfer type parameter K_{orbo} are given in Table 3.

Additive uncertainties due to inherent instrumental asymmetries mostly cancel out when extracting the parameters through the combination of data with opposite beam polarization, obtained by the fast flipping of the polarized ion source. The sensitivity of Monitor-1 to the beam polarization induces an additive error mainly on the A_{oono} parameter. These effects have been evaluated and are smaller than the statistical errors and have been ignored.

For A_{oono} there are abundant data [10,16,17,22-25] which is reflected in the excellent agreement between different PSA predictions and potential models. The quality of the A_{oono} TRIUMF data [16] between 70° to 100° at 425 and 495 MeV has been in doubt for a long time and the possiblility of a data-taking error has now been acknowledged by one of the authors [42] after the precise measurements of [10,24]. Our data also disagree with those earlier TRIUMF results, confirming any decision to reject the questionable data of [16].

There are only two series of experimental polarization transfer results with comparable errors in the energy and angular range of the present measurement: data from TRIUMF [9,16] for K_{onno}, $K_{os''ko}$ and $K_{os''so}$ at 220, 325, 425 and 495 MeV; and results from LAMPF [21,22] at 485 MeV on K_{onno}, $K_{os''so}$ and$K_{os''ko}$. The closest LAMPF data at higher energy are at 647 MeV. There are almost no results between 495 MeV and 647 MeV, a deficiency which is remedied by our new data. As the K_{onno} results from [16] were extracted from the same measurements used to obtain the incorrect A_{oono} values at 425 and 495 MeV, it was essential to remeasure K_{onno} in that energy range.

Since our data and those from TRIUMF and LAMPF were obtained at somewhat different incident kinetic energies, they cannot be compared directly. Our energies are in-between the TRIUMF energies. Therefore they allow the energy dependence of the four spin parameters to be better determined: one observes that both PSA analyses describe the energy dependence quite well for the $K_{os''so}$ and $K_{os''ko}$ parameters, but not for K_{onno}, especially below 472 MeV. A readjustment of the PSA will be necessary. Our data are in complete disagreement with the six TRIUMF data points at 516 MeV on K_{onno} and $K_{os''so}$ [8]. These data needed normalization factors as large as 2-3 in various PSA analyses and can now be safely eliminated.

In conclusion, these new data, which represent the first part of our *np* experimental program at PSI, have added new results and clarified important questions about the quality of existing data in the 260-538 MeV energy range. Existing PSA have been checked and will need further adjustment to improve the energy dependence of the K_{onno} parameter. The Bonn potential provides a better description of the present data than the Paris potential.

Acknowledgements. We thank the Paul Scherrer Institute for its valuable technical assistance. Thanks are also due to P. Extermann for his continuous support and encouragement during the course of this experiment. Many useful discussions with L.G. Greeniaus are here acknowledged. We also would like to thank the technical staff of the University of Geneva. This work was supported by the Swiss National Science Foundation and the German BMBF.

References

1. C. Lechanoine-Leluc, F. Lehar, Rev. Mod. Phys. **65**, No.1 (1993) 47
2. J. Bystricky et al., J. Phys. (Paris) **39** (1978) 1
3. E. Aprile et al., Phys. Rev. Lett. **46** (1981) 1047 and Phys. Rev. D**40** (1989) 22
4. C.D. Lac et al., J. Phys. France **51** (1990) 2689
5. J. Ball et al., submitted to Eur. Phys. J.
6. A. Ahmidouch et al., SPIN96, Amsterdam; 12th International Symposium on the high-energy spin physics, edited by C.W. de Jager, T.J.Ketel, P.J.Mulders, J.E.J. Oberski, M. Oskam-Tamboezer, World Scientific, page 588 (1997) and A. Ahmidouch et al., PANIC96, Williamsburg; 14th International Conference on Particles and Nuclei, edited by C.E. Carlson, J.J. Domingo, World Scientific, page 343 (1997)
7. N. Naef, PhD thesis, University of Geneva (1996) No2832
8. C. Amsler et al., Nucl. Instr. and Meth. **144** (1977) 401
9. D. Axen et al., Phys. Rev. C**21** (1980) 998
10. D. Bandyopadhyay et al., Phys. Rev. C**40** (1989) 2684
11. J. Ball et al., Nucl. Phys. B**286** (1987) 635
12. J. Ball et al., Nucl. Phys. A**559** (1993) 489
13. T.S. Bhatia et al., AIP conference Proceedings No69 (1981) 123
14. O. Chamberlain et al., Phys. Rev. **105** (1957) 288
15. D. Cheng et al., Phys. Rev. **163** (1967) 1470
16. A.S. Clough et al., Phys. Rev. C**21**, (1980) 988
17. C.A. Davis et al., Phys. Rev. C**53** (1996) 2052
18. R.T. Siegel et al., Phys. Rev. **101** (1956) 838
19. K-C. Leung, PhD thesis UCRL-19705 (1970)
20. J.A. Marshall et al., Phys. Rev. C**34** (1986) 1433
21. H.K. McNaughton et al., Phys. Rev. C**46** (1992) 47
22. M.W. McNaughton et al., Phys. Rev C**48** (1993) 256
23. M.W. McNaughton et al., Phys. Rev. C**53** (1996) 1092
24. C.R. Newson et al., Phys. Rev. C**39** (1989) 965
25. S.C. Wright et al., Phys. Rev. **175** (1968) 1704
26. R.A. Arndt et al., Phys. Rev. D**45** (1992) 3995, SAID solution FA95
27. J. Bystricky et al., J. Phys. (Paris) **48** (1987) 199 and updated solution in 1997
28. M. Lacombe et al., Phys. Rev. C**21** (1980) 861
29. R. Machleidt et al., Phys. Reports **149** (1987) 1
30. A. Teglia, PhD thesis, University of Geneva (1997) No2948
31. J. Arnold et al., Nucl. Instr. and Meth. in Phys. Res. A **386** (1997) 211
32. J. Arnold et al., submitted to Eur. Phys. J.
33. D.L. Prout et al., Phys. Rev. Lett. **76** (1996) 4488
34. P. Marmier et al., Nucl. Instr. and Meth. B**47** (1990) 37
35. Ch. Brönnimann et al., Nucl. Instr. and Meth. in Phys. Res. A **343** (1994) 331
36. A. Ahmidouch et al., Nucl. Instr. and Meth. A **326** (1993) 538
37. G. Charpak et al., Nucl. Instr. and Meth. **62** (1968) 235
38. D. Besset et al., Nucl. Instr. and Meth. **148** (1978) 129
39. P. Murdoch et al., Computer Technical note CTN-90-04 PSI (1990)
40. D. Besset et al., Nucl. Instr. and Meth. **166** (1979) 515
41. W.T. Eadie et al., Statistical Methods in experimental physics, North Holland Publishing Company (1970)
42. D.V. Bugg, Phys. Rev. C**41** (1990) 2708